Journal of Power Sources Advances 25 (2024) 100135

Contents lists available at ScienceDirect

Journal of Power Sources Advances

journal homepage: www.sciencedirect.com/journal/journal-of-power-sources-advances

MgO coated P2-$Na_{0.67}Mn_{0.75}Ni_{0.25}O_2$ layered oxide cathode for Na-Ion batteries

Cornelius Gauckler [a], Gints Kucinskis [a,b], Lukas Fridolin Pfeiffer [a], Abdelaziz A. Abdellatif [a], Yushu Tang [d,e], Christian Kübel [c,d,e], Fabio Maroni [a], Ruihao Gong [a], Margret Wohlfahrt-Mehrens [a,c], Peter Axmann [a], Mario Marinaro [a,*]

[a] Zentrum Für Sonnenenergie Und Wasserstoff Forschung Baden-Württemberg (ZSW), Helmholtzstraße 8, 89081, Ulm, Germany
[b] Institute of Solid State Physics, University of Latvia, Kengaraga Street 8, Riga, LV-1063, Latvia
[c] Helmholtz Institute Ulm (HIU) Electrochemical Energy Storage, Helmholtz Str. 11, D-89081, Ulm, Germany
[d] Institute of Nanotechnology (INT), Karlsruhe Institute of Technology (KIT), Hermann-von-Helmholtz-Platz 1, 76344, Eggenstein-Leopoldshafen, Germany
[e] Karlsruhe Nano Micro Facility (KNMFi), Karlsruhe Institute of Technology (KIT), Hermann-von-Helmholtz-Platz 1, 76344, Eggenstein-Leopoldshafen, Germany

ARTICLE INFO

Keywords:
Coating
Layered oxide
Magnesium
Batteries
Sodium

ABSTRACT

In this study, we propose an effective strategy to improve the electrochemical performance of a P2-$Na_{0.67}Mn_{0.75}Ni_{0.25}O_2$ (P2-MNO) cathode material for Na-ion batteries based on MgO surface coating. The MgO coating, with a thickness of ~20–50 nm, is obtained by means of a facile wet-chemistry approach followed by heat treatment carried out at comparatively low temperatures (400–500 °C) in order to avoid possible Mg doping in the bulk of the P2-MNO. Detailed electrochemical investigations demonstrate improved electrochemical performance of the MgO-coated material (M-P2-MNO) in comparison to pristine bare one at both room and elevated (40 °C) temperatures. *Operando* differential electrochemical mass spectroscopy (DEMS) demonstrate that the MgO coating is effective in suppressing unwanted gas evolution due to side reactions thus stabilizing the cathode/electrolyte interface.

1. Introduction

Rechargeable batteries are the go-to energy storage technology not only for portable electronics, but also electric vehicles and stationary energy storage applications. Although Lithium-ion batteries (LIBs) currently dominate the market, sodium-ion batteries (NIBs) are increasingly gaining attention as a more sustainable and potentially cheaper alternative [1]. Among the advantages of NIBs are the high abundance of sodium (the sixth most abundant element in the earth crust), similar manufacturing requirements to LIBs (can be used as a technological drop-in using current LIBs manufacturing techniques) and the ability to replace copper with aluminum as current collector on the anode side [2]. The production cost of NIBs is expected to be 10–20 % lower compared to LIBs, further strengthening the case of NIBs as a promising alternative battery chemistry for energy storage and mobility [2].

Among various promising cathode materials for NIBs, P2-type Na-layered transition metal oxides with the stoichiometry $Na_{2/3}MO_2$ (M = transition metals), offer one of the highest discharge capacities and energy densities [3]. Generally, Na_xMO_2 layered oxides consist of MO_6 octahedral sheets ordered in different orientations, thus generating a wide crystal family [4,5]. Currently investigated structures of $Na_{2/3}MO_2$ include P2-, P′2-, O2-, P3-, O3-, OP4- phases according to Delmas' notation, with P and O representing the prismatic (P) or octahedral (O) alkali ion sites. The numbers denote the amount of MO_6 slabs in the repeating units and the prime symbol signifies a distortion of the unit cell [6,7]. Compared to the O3 phase, the P2 polymorph of Na_xMO_2, with its ABBA stacking sequence, typically formed at $x \approx 0.7$, has faster Na^+ diffusion kinetics, ensuring excellent rate capability [5,7,8].

However, despite its attractive Na^+ mobility, P2-type $Na_{2/3}MO_2$ materials are often plagued by suboptimal cycling stability. This is mainly related to three reasons: i) undesired transformations of the crystal lattice, ii) irreversible anion redox reactions and iii) presence of Jahn-Teller active Mn^{3+} in the lower end of their electrochemical cycling window. In detail, $Na_{2/3}MO_2$ materials can undergo complex phase transformations during de-/sodiation, leading to rapid capacity

* Corresponding author.
E-mail address: mario.marinaro@zsw-bw.de (M. Marinaro).

https://doi.org/10.1016/j.powera.2024.100135
Received 15 September 2023; Received in revised form 19 December 2023; Accepted 6 January 2024
Available online 14 January 2024
2666-2485/© 2024 Published by Elsevier Ltd. This is an open access article under the CC BY-NC-ND license (http://creativecommons.org/licenses/by-nc-nd/4.0/).

fade. Gliding of the P2-type metal oxide planes is ruled by electrostatic repulsion of the oxygen atoms and leads to the complex phase transitions [9]. For instance, P2-P′2, P2-O2 and the formation of intermediate OP4 or Z phases have all been reported [7,10]. Furthermore, phase transformations are often accompanied by significant volume changes which can result in particle cracking and associated capacity loss [11,12]. In addition, anion redox reactions (e.g. between O^{2-} and $(O_2)^{n-}$) can influence the general electrode performance of P2-type cathode materials as well. On the one hand, if the anion redox reactions are reversible, additional cathode capacity can be observed, as shown in various studies on both LIBs [13] and NIBs including the P2-type Na_xMO_2 [12,14]. Irreversible anion redox reactions, on the other hand, can also lead to O_2 release leading to side reactions with the electrolyte, causing permanent changes of the crystal structure and degradation of the active material [15]. Lastly, the Jahn-Teller active Mn^{3+} is known to cause strain and stress on the active material due to an increased structural disorder [16].

To restrict the intrinsic poor cycling stability of P2-type Na_xMO_2, coating the Na_xMO_2 particles with a protective layer (surface coating) is an effective approach, which has been widely employed in LIBs. Interestingly, a surface coating can serve as a multifunctional layer, protecting the cathode material particles from various unfavorable factors including hydrofluoric acid (HF) attack, parasitic reactions between electrode and electrolyte, as well as phase transitions, loss of lattice oxygen and formation of micro-cracks in the cathode material crystals [17–19].

Metal oxide coatings often have high mechanical strength and fracture-toughness, not only ensuring a stable artificial CEI (Cathode Electrolyte Interphase), but also mitigating the lattice expansion and preventing electrode cracking [18,20]. Plenty of metal oxide and ceramic coatings have been developed (MgO, Al_2O_3, ZnO, CuO and other) [21–28] and employed on various cathode material surfaces, delivering improved long-term cycling stability, frequently also with boosted rate capability.

To achieve a reliable and robust surface layer, different technologies, such as atomic layer deposition (ALD) and wet chemical methods, can be employed. ALD can yield very homogenous coatings but is relatively complicated and expensive to be scaled up for industrial production. In contrast, a wet chemical approach is simpler, as the coating process can be conducted as an additional step following the synthesis of the pristine material, which makes it a candidate for scaled-up cathode material production. However, wet chemical treatment can easily end up with a 'fuzzy line' between doping and coating on the surface of the cathode particles [19]. Several groups have attempted to treat P2-type sodium transition metal oxides by wet-chemical methods and have detected, for instance, simultaneous coating of MgO and doping by Mg^{2+} on the transition metal sites [22]. Although not always explicitly discussed, this effect might be present in many more studies [21–23,28]. Meanwhile, similar results have been obtained with ZnO and CuO coatings [26,27].

In this study, a layered P2-$Na_{0.67}Mn_{0.75}Ni_{0.25}O_2$ (P2-MNO) cathode material is prepared via a combined co-precipitation and solid state method. Hereafter, an MgO surface-coated P2-MNO cathode material (M-P2-MNO) is successfully obtained by a wet-impregnation process followed by calcination at moderate temperatures. The MgO-surface coating is homogeneously distributed on the P2-MNO spherical particles and significantly improves the cycling stability of the latter. Detailed *operando* and *ex-situ* characterization techniques reveal that the surface coating can simultaneously reduce the amount of cracks and restrict the evolution of gases such as O_2 and CO_2 during galvanostatic cycling.

2. Experimental

2.1. Material synthesis

2.1.1. Synthesis of pure P2-$Na_{0.67}Mn_{0.75}Ni_{0.25}O_2$

P2-$Na_{0.67}Mn_{0.75}Ni_{0.25}O_2$ (P2-MNO) is synthesized via a 2-step method, which is detailed in our previous work [29,30]. Briefly, a $Mn_{0.75}Ni_{0.25}(OH)_2$ precursor (synthesized via co-precipitation in a continuous stirred tank reactor (CSTR, $V = 1$ L)) is mixed with an aqueous sodium hydroxide (NaOH, Carl Roth) solution (7 mol/L) and calcined at 900 °C for 12 h in air. The surface area of the P2-MNO is of 0.28 m^2/g.

2.1.2. Synthesis of MgO-coated P2-$Na_{0.67}Mn_{0.75}Ni_{0.25}O_2$

MgO surface-coated P2-MNO (M-P2-MNO) is prepared by a 3-step process. In detail, P2-MNO, is first synthesized as mentioned above, followed by the dropwise addition of an aqueous magnesium nitrate (1 wt% MgO equivalent) ($Mg(NO_3)_2$, Sigma-Aldrich) solution. Afterwards, the mixture is calcined at 400 °C in a Nabertherm batch furnace for 4 h in air. After calcination and cooling to 200 °C, P2-MNO and M-P2-MNO are quickly transferred into a vacuum glass oven (BÜCHI Labortechnik GmbH, Germany) at 200 °C under dynamic vacuum ($< 3 \bullet 10^{-5}$ mbar) for 12 h. Finally, the dried powders are transferred into an Ar-filled Glovebox (MBraun $H_2O < 0.1$ ppm, $O_2 < 0.1$ ppm) and stored there for further characterization and testing.

2.2. Material characterization

Powder X-ray diffraction (PXRD) patterns are recorded in Bragg-Brentano geometry in the range $2\theta = 10$–$90°$ and a step size of 0.01° on a D8-Advance (Bruker) diffractometer using $Cu_{K\alpha1}$ X-ray tube ($\lambda = 1.54056$ Å) and a XE-T detector. The obtained PXRD data is further analyzed by Rietveld refinement using Topas V6 software. The elemental composition of the as-synthesized material powder is characterized by inductively coupled plasma optical emission spectroscopy (ICP-OES, Spectro Arcos SOP). Material morphology is observed by scanning electron microscopy (SEM), using a Leo Gemini 1530 VP instrument (Zeiss), where images are generated at accelerating voltage of 5 kV with an Everhart-Thornley-SE-Detector.

Transmission electron microscopy (TEM) analysis has been performed using an aberration corrected Themis 300 (ThermoFischer Scientific) probe, operated at 300 kV and equipped with a high-angle annular dark field (HAADF) detector (Fischione), a Ceta CCD camera (ThermoFischer Scientific) and a Super-X EDX detector (ThermoFischer Scientific). The collection angle for acquiring the STEM-HAADF images was 74–200 mrad. The convergence angle was set to 30 mrad and the screen current was about 170 pA for image acquisition and EDS mapping. For TEM image acquisition, the C2 aperture was set to 150 μm and the spot size was set to 4. Data processing has been performed using the Velox software package (ThermoFischer Scientific). TEM samples have been prepared by focused ion beam (FIB) technique using a Strata 400S (FEI Company). A carbon layer was first deposited on the M-P2-MNO particle surface, as a protective coating. Cross-section FIB preparation was initially performed at 30 kV and the final polishing at 2 kV.

2.3. Electrode preparation and electrochemical measurements

Electrodes are prepared inside an Ar-filled Glovebox (Mbraun ®). In detail, the as-synthesized active materials (P2-MNO or M-P2-MNO) are dry mixed with polyvinylidenefluoride (PVDF) binder and Super P® (Timcal) conductive carbon in a 84:8:8 weight ratio, in a mortar. Then, NMP (N-methyl-2-pyrrolidone) is added as solvent for preparing electrode slurries. After mixing for 3 h with a magnetic stirrer at 300 rpm, the slurry is coated onto an Al foil current collector via a doctor blade, resulting in a mass loading of ~4–5 $mg \bullet cm^{-2}$. The coated Al foil is then dried at 80 °C for 1 h. Disk electrodes (12 mm diameter) are punched and dried for 12 h at 130 °C under dynamic vacuum in a glass oven. Galvanostatic cycling experiments are performed using a VMP3 (Bio-Logic) multichannel potentiostat with 3-electrode Swagelok-type-T-cells assembled in an Ar-filled glovebox (Mbraun ®). Here, metallic sodium serves as counter and quasi-reference electrode. Circular Whatman GF/A glass fiber is used as separator and ~300 μL of a 1 M $NaPF_6$ (99.99 %,

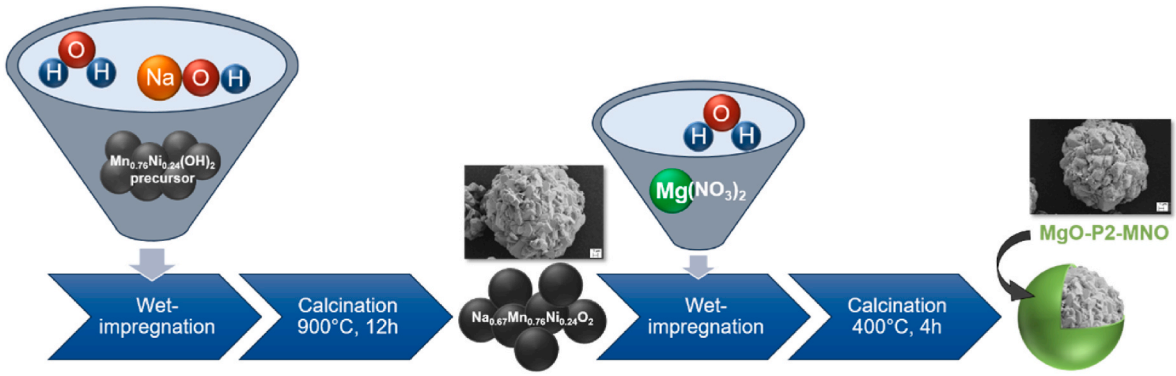

Fig. 1. Schematic figure of the synthesis process of the MgO-surface-coated P2-MNO cathode material.

Sigma-Aldrich) in propylene carbonate (PC) + 5 % fluoroethylene carbonate (FEC) solution is added as electrolyte. Cycling stability and rate capability of different cathode materials are evaluated by charging/discharging the corresponding T-cells at different current rates in the potential range of 2.00 V–4.30 V (vs. Na^+/Na). Galvanostatic Intermittent Titration Technique (GITT) measurements are carried out with a current pulse at C/100 rate (~24 μAh• g^{-1}) applied for 1 h, followed by a relaxation until the potential variation rate is below 5 mV•h^{-1} to analyze the kinetics of Na^+ diffusion.

To investigate the gas evolution during the charging/discharging processes of Na-ion batteries, a in-house online differential electrochemical mass spectrometer (DEMS) cell is designed and connected to the mass spectrometer (HPR40, HIDEN Analytical, UK) via a crimped capillary leak (Accu-Flow Calibrated Leak, VTI, USA) with a gas flow rate of 1 μl/min [31]. The cell consists of: i) two steps in the lower stainless steel plate to precisely arrange the Na foil disk and the separator layers and to contain the electrolyte. ii) Two holes are present in the upper stainless steel compartment. One is connected to the flushing Ar cylinder and the capillary leak via a T-connector and the other one for flushing gas outlet iii) The aluminium mesh and the stainless steel spring have been aligned above the perforated cathode to serve as a current collector and to keep a defined pressure on the electrode. iv) The Kel-F (Beichler + Grünenwald GmbH) cylinder and PEEK pieces around the screws have been used as insulators between the cathode and anode compartments. v) The whole cell was sealed with Viton O-rings (type FPM75, 2.5 mm cross-section and 28 mm ID, HUG Technik und Sicherheit GmbH, Germany). The cell inner volume is ≈ 9.2 ml. The working electrode preparation is described below. For this cell-setup a 12 mm working electrode, a 15 mm diameter Na-metal counter electrode, 2x GF/A separator and 450 μl 1 M $NaPF_6$ in PC + 5% FEC have been used. The DEMS cell is completely assembled in the glovebox then it is transferred outside the glovebox after closing the attached valve. The cell is connected to the mass spectrometer and the tubes are firstly evacuated to 10^{-3} mbar before opening the connecting valve. The electrochemical performance of the cell is tested using BaSyTech GmbH (Germany) and the ionic signals are simultaneously recorded by mass spectrometer.

3. Results and discussion

MgO-coated P2-MNO (M-P2-MNO) is obtained via a dropwise-wet-impregnation method, as schematically presented in Fig. 1. It is worth mentioning that a suitable Mg-salt is crucial for this method, because Mg-containing species like $MgCO_3$, MgO or $Mg(OH)_2$ are poorly or completely insoluble in common solvents, like H_2O or ethanol.

Thanks to his good solubility in water, we therefore chose $Mg(NO_3)_2$. The influence of different solvents and heat treatment temperatures on the corresponding M-P2-MNOs were also investigated to optimize the

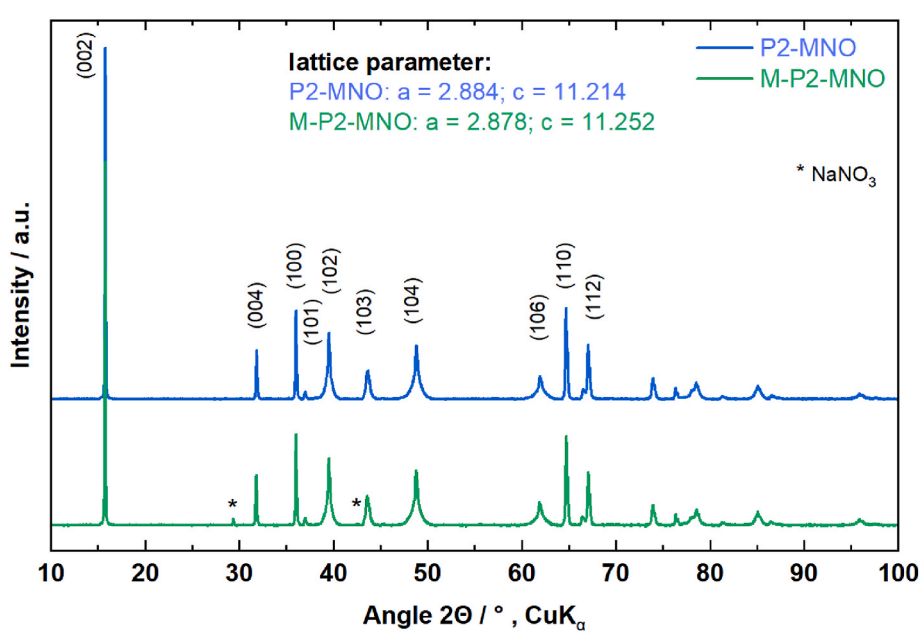

Fig. 2. X-ray diffraction patterns of the pristine P2-MNO and 1 wt% MgO-coated P2-MNO (M-P2-MNO) cathode materials.

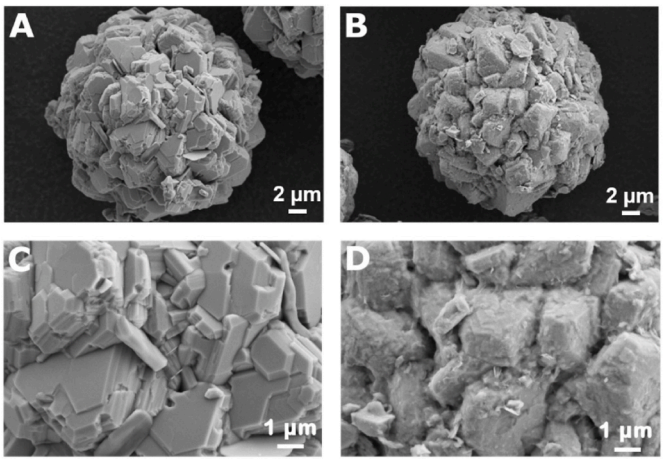

Fig. 3. SEM top-view images of pristine material P2-MNO (A and C) and 1 wt% MgO-coated sample (M-P2-MNO) (B and D).

coating conditions (Table S1).

As demonstrated by the XRD patterns in Fig. 2, the P2-type structure of pristine P2-MNO is preserved after MgO surface coating. However, some additional diffraction peaks with low intensity appear, which can be assigned to $NaNO_3$ (Table S4). Although $NaNO_3$ only starts to decompose at 450 °C [32], we chose moderate synthetic temperatures (< 500 °C) for MgO-coating, thus avoiding structural reorganization leading to the formation of mixed layered oxide (P2, P3) [30] and possibly preventing the integration of Mg^{2+} into transition metal positions, namely a bulk Mg^{2+}-doping process. In an ideal case, simultaneous Mg doping and MgO-surface coating can maximize the stability of the P2-type cathode materials [22]. Based on our previous results, calcination at higher temperatures (up to 900 °C) leads to crystalline MgO which is unevenly distributed on the particle surface. The absence of characteristic MgO reflections in Fig. 2 is likely due to its low amount, which might be below the detection limit. Furthermore, Rietveld refinements were carried out to reveal the respective variations of *a* and *c* lattice parameters due to the presence of MgO-coating (Table S3, Fig. S1). As expected, the *a* lattice parameter of the P2-MNO structure does not considerably change after MgO-surface-coating. Nevertheless, the observed *c* parameter of M-P2-MNO is higher in comparison with that of P2-MNO. The second annealing step for MgO-coating triggers a slight Na^+ loss from the P2-MNO structure, and leads to an increased electrostatic repulsion of the hexagonal oxygen layers, resulting in an increased *c* lattice parameter.

Additionally, scanning electron microscopy (SEM) is used to analyze and compare the morphology of pristine and MgO-coated P2-MNO. As demonstrated by Fig. 3, both samples show similar spherical polycrystalline particle shape with an average size of 20–25 µm. Fig. 3D shows substantial differences in the M-P2-MNO surface when compared to the bare MNO (Fig. 2C), suggesting that the coating was successfully applied.

To confirm the presence of the MgO coating and evaluate its

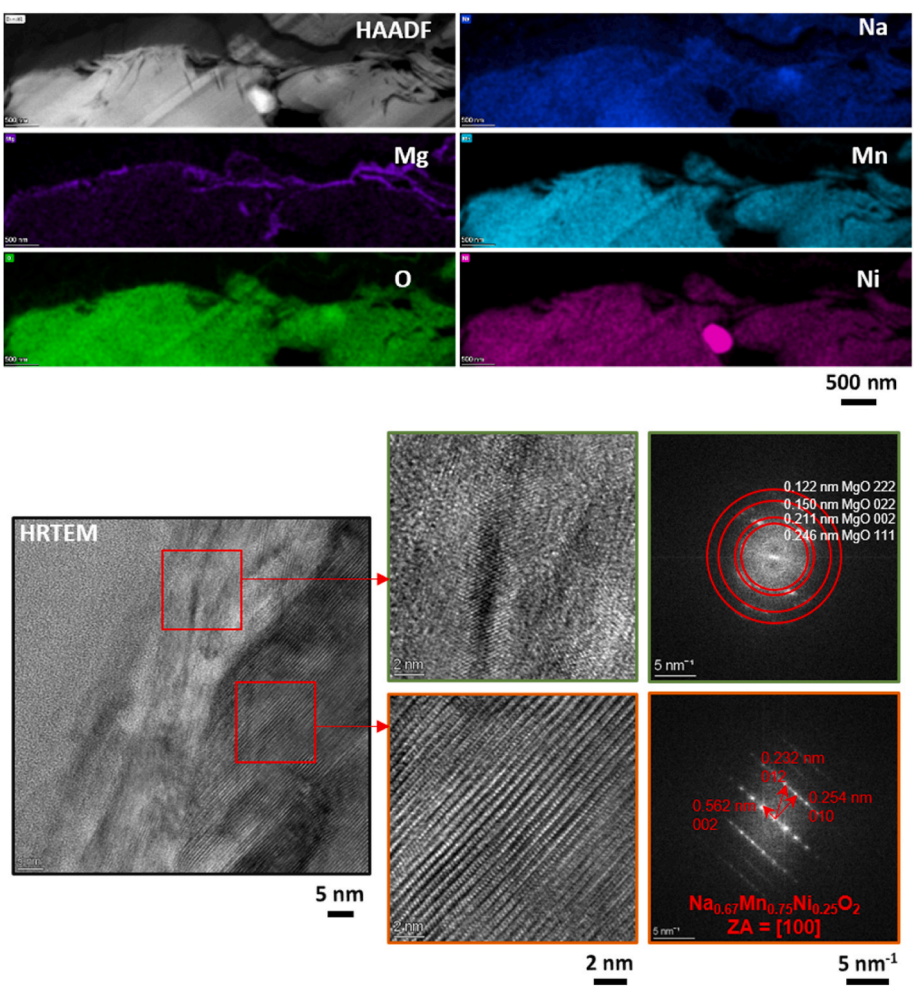

Fig. 4. HAADF-STEM overview image with STEM-EDX elementals maps and HRTEM of M-P2-MNO in agreement with $Na_{0.67}Mn_{0.75}Ni_{0.25}O_2$ and an MgO coating (raw images in supplementary info).

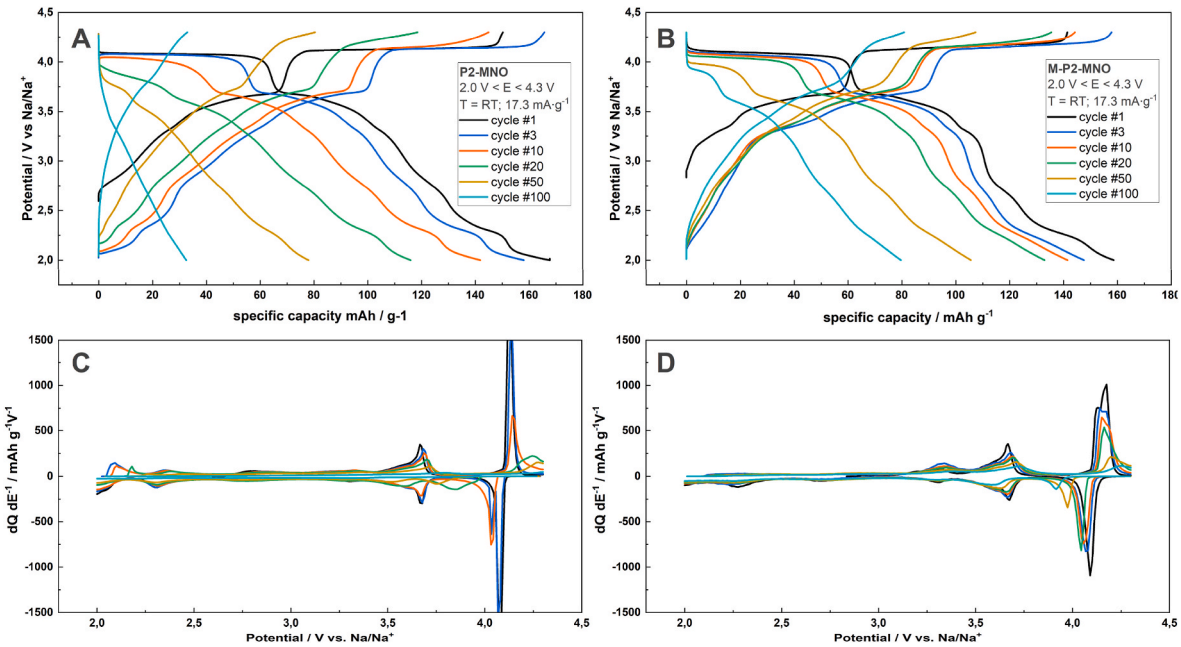

Fig. 5. Galvanostatic charge/discharge profiles (2.0 V < E < 4.3 V; T = RT; 17.3 mA•g^{-1}) of P2-MNO (A), M-P2-MNO (B) and the corresponding differential analyses of P2-MNO (C), M-P2-MNO (D).

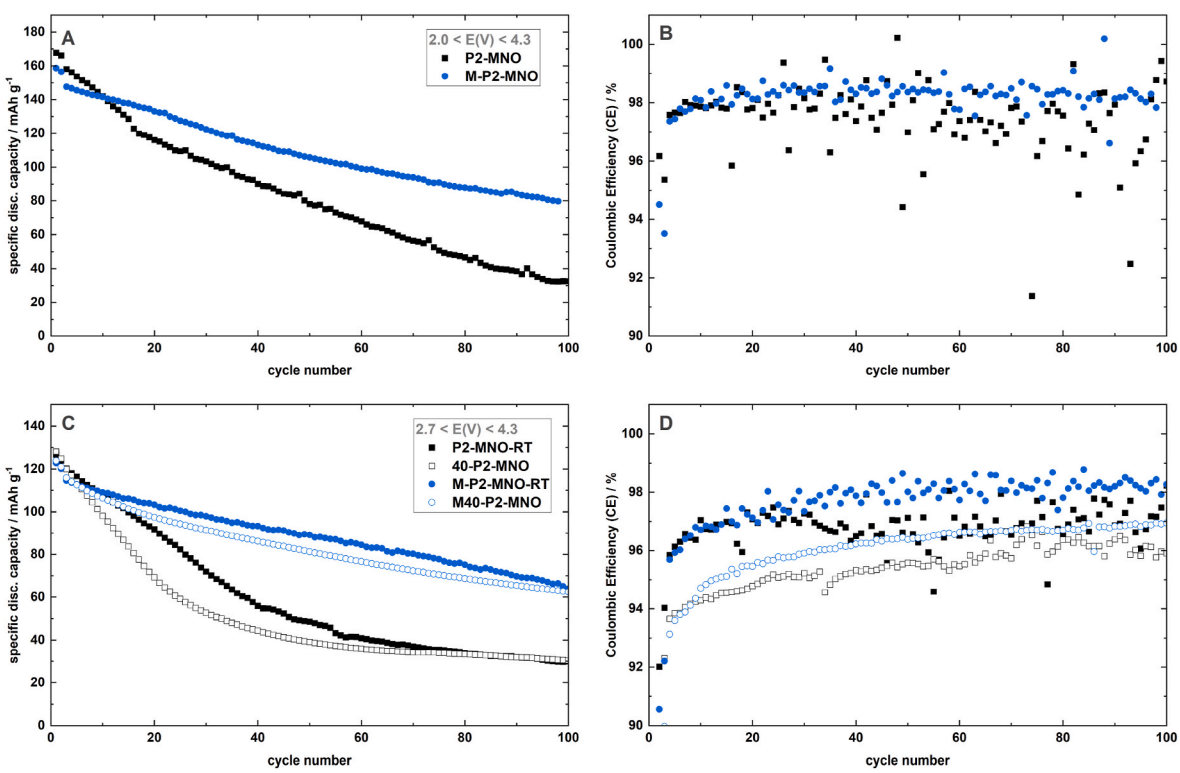

Fig. 6. Long-term cycling performance and coulombic efficiency of (A, B) P2-MNO and M-P2-MNO at T = 25 °C with a potential window of 2.0 < E(V) < 4.3 and (C, D) P2-MNO and M-P2-MNO at T = 40 °C with a potential window of 2.7 < E(V) < 4.3.

thickness, STEM-EDX mapping has been performed for M-P2-MNO. The results shown in Fig. 4 confirm the formation of a conformal thin surface film consisting of MgO with a thickness of ~20–50 nm around the polycrystalline secondary particles as well as some internal coating at gaps/cracks in the secondary particles. The MgO layer exhibits a fairly defined layer on the MNO particles without significant Mg doping well below the MNO surface. HRTEM analysis of the particles confirms the formation of MgO as a surface coating based on the observed lattice spacings and the crystal structure of the particles is in agreement with the basic $Na_{0.67}Mn_{0.75}Ni_{0.25}O_2$ structure. In addition to $Na_{0.67}Mn_{0.75}Ni_{0.25}O_2$, the EDX results show a Ni-rich area, presumably NiO, which we attributed to an impurity from the synthesis. As the XRD patterns did not show any characteristic reflection for NiO, we assume its amount to be low.

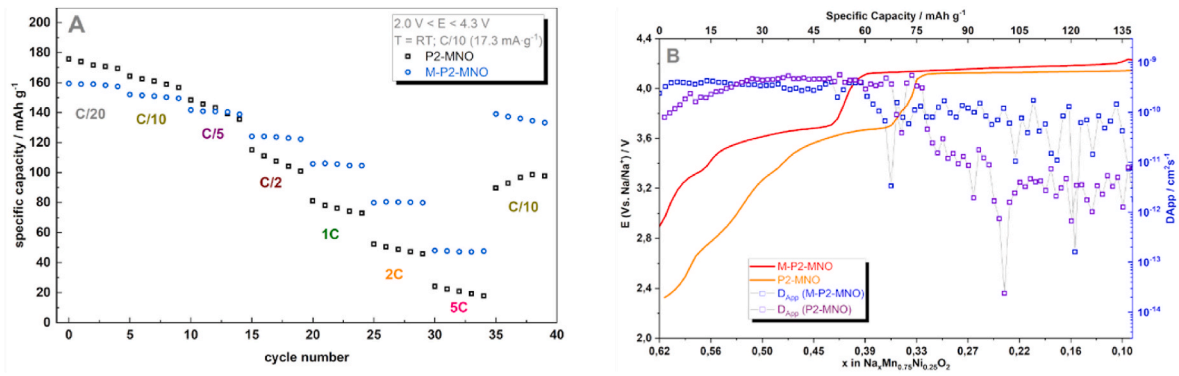

Fig. 7. Rate capability test of P2-MNO (black) and M-P2-MNO (blue) at current rates of C/20, C/10. C/5, C/2, 1C, 2C and 5C (A), and GITT measurement with the calculated apparent Na^+ diffusion coefficient of M-P2-MNO (B). (For interpretation of the references to color in this figure legend, the reader is referred to the Web version of this article.)

To assess the electrochemical performance, the P2-MNO and the M-P2-MNO were characterized by galvanostatic charge/discharge cycling at C/5 rate (1C = 173 mA•g^{-1}), with two formation cycles at C/10 rate in a Swagelok-type 3-electrode test setup. Charge and discharge profiles of selected cycles are shown in Fig. 5A and B. It can be inferred that the initial charge capacity of P2-MNO (150.3 mAh•g^{-1}, initial coulombic efficiency (CE) = 96.2%) is slightly higher than that of M-P2-MNO (142.9 mAh•g^{-1}, initial CE = 94.5%). The lower initial capacity of M-P2-MNO can be correlated to the hypothesis of a loss of Na and subsequent increase of the c-lattice parameter, as seen in the XRD. Here, both materials show similar galvanostatic profiles in which the potential increases gradually from OCV to E(V) = ~4.10 (vs. Na^+/Na), followed by a plateau at E(V) = 4.2 (vs. Na^+/Na). Interestingly, the MgO-coated material exhibits a higher specific capacity than P2-MNO from cycle 15 onwards (Fig. 6A). Furthermore, M-P2-MNO delivers less fluctuating capacity values after each cycle as well as a slightly higher CE compared to P2-MNO (Fig. 6B). Finally, after 100 cycles, M-P2-MNO still holds a considerable capacity of 81 mAh•g^{-1} (capacity retention of 51%) while the capacity of P2-MNO fades to 33 mAh•g^{-1} (capacity retention of 19%).

Differential analysis of the P2-MNO (Fig. 5C) and M-P2-MNO (Fig. 5D) galvanostatic profiles is conducted to investigate the oxidation and reduction pathways of each material. For both materials, the reversible peak couples in the region of 3.2 ≤ E(V vs. Na^+/Na) ≤ 3.9 are attributed to the redox of Ni^{2+}/Ni^{4+} [33]. As the potential rises, the anodic and cathodic peaks in the region of 4.0 ≤ E(V vs. Na^+/Na) ≤ 4.30 are assigned to the P2-O2 phase transition [34]. The peak shapes of both materials undergo continuous change with the proceeding cycles in this potential range. For the P2-MNO, an initially sharp, high-intensity peak with a capacity of ~74 mAh•g^{-1} is detected in the first cycle. The initial capacity of the M-P2-MNO has the same value (74 mAh•g^{-1}) but the peak appears to be broader and with a significantly lower intensity. A clear explanation for such dissimilarity is still missing and subject to further investigation. In the potential range below E < 2.50 V(vs. Na^+/Na), the Mn^{3+}/Mn^{4+} redox couple is active [35]. For the P2-MNO, the corresponding Mn^{3+}/Mn^{4+} peaks are less intense compared to its Ni-related peaks. Of note, the Mn-redox peaks are further reduced in intensity or even absent in M-P2-MNO.

The capacity loss for both materials over 100 cycles mainly stems from the region of the P2-O2 phase transition. While the initial capacity loss of the "high potential plateau" (cycle #1 to #3) is similar in both materials, the capacity decays during cycling for P2-MNO is higher than that for M-P2-MNO. In detail, the capacity retention has already decreased by 30% in P2-MNO after only 20 cycles, in clear contrast with M-P2-MNO (15%), from which the capacity drop is less severe. It is also worth noting that P2-MNO, unlike M-P2-MNO, suffers from a continuous capacity loss located in the solid solution regime (2.0 < E(V vs. Na^+/Na) < 4.0).

The electrochemical performance of the M-P2-MNO and P2-MNO is also evaluated at T = 40 °C and compared in the aspect of capacity retention (Fig. 6C). Additionally, the potential window is adjusted from 2.0 < E (V vs. Na^+/Na) < 4.3 to 2.7 < E (V vs. Na^+/Na) < 4.3 in order to better reflect the expected behavior in a full cell. A higher operating temperature is generally a double-edged sword for the performance of electrode materials for metal-ion batteries. On the one hand, it tends to improve charge transfer kinetics within the cell [36], so the initial charge capacity increased at T = 40 °C for P2-MNO by 5 mAh•g^{-1} and for M-P2-MNO by 2.4 mAh•g^{-1}. On the other hand, parasitic side reactions can be facilitated at elevated temperatures, which lead to faster capacity decay [37]. Although this increasing decay rate due to the higher cycling temperature is observed in both materials in this study, it is worth noting that the capacity retention (after 100 cycles) of M-P2-MNO (~53%) is higher than its uncoated counterpart (~24%) at T = 40 °C. Furthermore, the coulombic efficiency of M-P2-MNO remains higher than the P2-MNO (~96% vs. ~95%) at T = 40 °C (Fig. 6D).

Besides reliable stability upon charge/discharge, the high rate capability of battery materials is another important parameter, especially in view of high-power applications. Therefore, the rate performances of P2-MNO and M-P2-MNO have been assessed and compared (Fig. 7A). As expected, the capacities for both samples decrease as the current density increases. At comparatively low current rates (C/20 to C/5, 1C = 173 mA•g^{-1}), the P2-MNO shows higher capacity. At higher rates (C/5 to 5C, Table S4), the M-P2-MNO cathode outperforms P2-MNO in terms of specific capacity and higher stability. That does not necessarily mean that the M-P2-MNO has better kinetics overall. Indeed, by looking at the control cycles (last five cycles at C/10) it is evident that only the M-P2-MNO is capable of achieving the same C/10 capacity as at the beginning of the test. In contrast, the capacity of the baseline material, namely P2-MNO, fades continuously during the whole rate test and cannot achieve its original capacity at C/10 afterwards, thus suggesting stronger aging effects as also seen in Fig. 6 A-D.

To have a better understanding of the kinetics of the two electrode materials, GITT experiments were carried out with the aim of extrapolating the apparent Na^+ diffusion coefficient (D_{App}). The sodium-ion apparent diffusion coefficient can be obtained by the following expression, as derived from the second Fick's law [38]:

$$D_{App,} = \frac{4}{\pi\tau}\left(\frac{m_B V_M}{M_B S}\right)^2\left[\frac{\Delta Es}{\Delta E_t}\right]^2\left(\tau \ll \frac{L^2}{D_{app}}\right),$$

with D_{App} = calculated diffusion coefficient, τ = duration of the current pulse, m_B = mass of the active material, M_B atomic weight of component B, S = electrochemical area of the sample-electrolyte interface, ΔE_s = change of equilibrium potential, ΔE_t = change of cell potential during the current pulse, neglecting the IR drop, L = diffusion length. Fig. 7B presents the evolution of D_{App} during the first charge of the M-P2-MNO

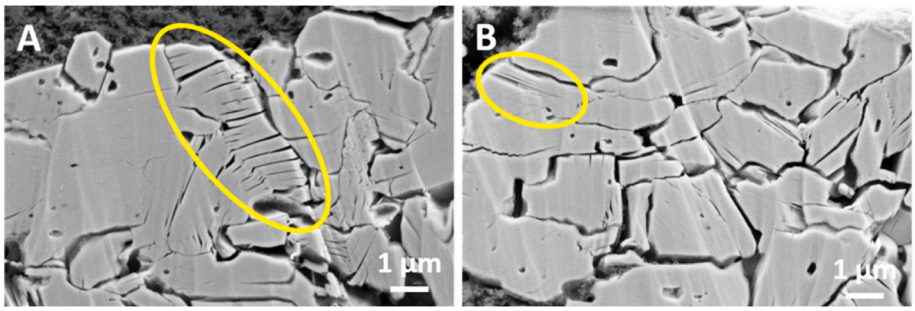

Fig. 8. SEM images (cross-section (A, B)) of cycled P2-MNO (A) and M-P2-MNO (B) electrodes.

cathode with a current pulse of C/100. During the solid-solution domain, namely in the OCV < E (V vs. Na^+/Na) < 4.10 range, the D_{App} is relatively constant with values in the magnitude of 10^{-9} cm^2 s^{-1}, comparable to the P2-MNO material, as previously reported [29]. In theory, the Na^+ diffusivity of M-P2-MNO can be expected to be lower than that of the non-coated P2-MNO sample because of the low ionic conductivity of MgO. However, at least for the first charge, the low ionic conductivity of MgO seems not significantly hinder the diffusion of Na-ions. We also here note that the M-P2-MNO shows greater D_{App} value during the P2-O2 phase transition, namely in the potential range 4.10 < E (V vs. Na^+/Na) < 4.30. However, the D_{App} values in the P2-O2-region need to be treated very carefully since the assumptions of Fick's law do not account for phase transitions.

Given that one of the main causes of irreversible capacity loss in the high potential region can be related to an irreversible evolution of O^{2-}/O_2^{n-}/O_2 [39], *operando* DEMS was used to investigate the gas evolution of the two different cathode materials and to better understand the reasons for degradation. Furthermore, oxygen release from layered oxide cathode materials may result in reactive oxygen species like singlet oxygen, which could oxidize the conductive carbon in the electrode or the electrolyte solvent to form CO_2[40–42]. The high reactivity of these intermediate oxygen species may explain the controversial data reported in literature, which may [43–45] - or may not [46–48] - detect O_2 evolution via DEM. It is worth mentioning that gas formation might result in a surface densification which would hinder Na^+ intercalation [45]. Oxygen (O_2; m/z = 32) and carbon dioxide (CO_2; m/z = 44) evolution has therefore been investigated for both materials (P2-MNO & M-P2-MNO) during the initial 3 charge/discharge cycles as presented in Fig. S3. DEMS results show a clear indication of CO_2 as well as O_2 evolution for the P2-MNO during the first and second cycle. The targets of the redox-inactive MgO surface coating are to reduce the above-mentioned side reactions and to stabilize the interface. Neither CO_2 nor O_2 evolution were detected from the MgO-surface coated material (M-P2-MNO), even in a wider voltage window (2.0 < E (V vs. Na^+/Na) < 4.3) thus suggesting a successful shielding of the particles from direct contact with the electrolyte, which avoids side reactions.

To gain further insight into the degradation mechanism at the electrode scale, post-mortem SEM analysis (after cycle #20) has been performed on both cathodes.

From the view of the cross-section, both cathode material particles exhibit visible cracks on the surface and within the bulk (Fig. 8). Notably, the cracks on the surface of P2-MNO appear slightly more severe than on M-P2-MNO. Previous studies have already pointed out that the strain induced by the P2-O2 phase transition, which involves a large volume change (> 20%) [25], plays an important role in crack formation [49]. It has also been reported that oxygen loss, as well as the simultaneous surface reconstruction, contributes to microcracks nucleation at the surface of cathode material particles [37], which is in accordance with the findings from the DEMS investigations in our study.

4. Conclusion

In this work, a homogeneous MgO surface coating has been successfully applied to the layered cathode material P2-$Na_{0.67}Mn_{0.75}Ni_{0.25}O_2$ (P2-MNO) for NIBs. The facile wet-chemical approach under mild temperature conditions leads to an MgO film (~20–50 nm thickness) covering the polycrystalline P2-MNO particles. The coating significantly improves the capacity retention of the P2-MNO cathode material from 19% to 51% after 100 galvanostatic charge/discharge cycles at room temperature. The surface coating is able to improve the electrodes cycle life even under more severe cycling conditions (T = 40 °C). Moreover, our *operando* DEMS results point out that the MgO coating is effective in suppressing unwanted gas evolution due to side reactions thus stabilizing the cathode/electrolyte interface.

CRediT authorship contribution statement

Cornelius Gauckler: Writing – review & editing, Writing – original draft, Methodology, Investigation, Formal analysis, Data curation. **Gints Kucinskis:** Writing – review & editing, Writing – original draft, Investigation, Data curation, Conceptualization. **Lukas Fridolin Pfeiffer:** Writing – review & editing, Writing – original draft, Data curation. **Abdelaziz A. Abdellatif:** Writing – original draft, Methodology, Investigation, Formal analysis, Data curation. **Yushu Tang:** Writing – original draft, Investigation, Formal analysis, Data curation. **Christian Kübel:** Writing – review & editing, Supervision, Resources, Project administration. **Fabio Maroni:** Writing – review & editing, Writing – original draft, Methodology, Formal analysis, Data curation. **Ruihao Gong:** Writing – review & editing, Methodology. **Margret Wohlfahrt-Mehrens:** Writing – review & editing, Funding acquisition. **Peter Axmann:** Writing – review & editing, Methodology, Funding acquisition. **Mario Marinaro:** Writing – review & editing, Supervision, Resources, Project administration, Funding acquisition, Conceptualization.

Declaration of competing interest

The authors declare that they have no known competing financial interests or personal relationships that could have appeared to influence the work reported in this paper.

Data availability

Data are made available at this repository: 10.5281/zenodo.8120332

Acknowledgments

This work contributes to the research performed at Center for Electrochemical Energy Storage Ulm-Karlsruhe (CELEST) and was funded by the Deutsche Forschungsgemeinschaft (DFG, German Research Foundation) under Project ID 390874152 (POLiS Cluster of Excellence) and by the German Federal Ministry of Education and Research (BMBF) in

the project TRANSITION (03XP0186C). Gints Kucinskis acknowledges Latvian Council of Science project "Advanced polymer – ionic liquid composites for sodium-ion polymer batteries", project No. LZP-2020/1–0391. Institute of Solid-State Physics, University of Latvia as the Centre of Excellence has received funding from the European Union's Horizon 2020 Framework Program H2020-WIDESPREAD-01-2016-2017-TeamingPhase2 under grant agreement No. 739508, project CAMART2. We would like to thank Claudia Pfeifer, Fabian Regnet and Ildiko Lüdeking from ZSW for the SEM measurements and the helpful discussion regarding the change in particle morphology. Data is available at [50].

Appendix A. Supplementary data

Supplementary data to this article can be found online at https://doi.org/10.1016/j.powera.2024.100135.

References

[1] D. Karabelli, S. Singh, S. Kiemel, J. Koller, A. Konarov, F. Stubhan, R. Miehe, M. Weeber, Z. Bakenov, K.P. Birke, Front. Energy Res. 8 (2020).
[2] K.M. Abraham, ACS Energy Lett. 5 (2020) 3544.
[3] J. Xiao, X. Li, K. Tang, D. Wang, M. Long, H. Gao, W. Chen, C. Liu, H. Liu, G. Wang, Mater. Chem. Front. 5 (2021) 3735.
[4] a) C. Delmas, J. Braconnier, C. Fouassier, P. Hagenmuller, Solid State Ionics 3–4 (1981) 165;
b) J.M. Paulsen, J.R. Dahn, Solid State Ionics 126 (1999) 3;
c) F. Capitaine, Solid State Ionics 89 (1996) 197.
[5] J.H. Stansby, N. Sharma, D. Goonetilleke, J. Mater. Chem. A 8 (2020) 24833.
[6] C. Delmas, C. Fouassier, P. Hagenmuller, Phys. B+C 99 (1980) 81.
[7] D.H. Lee, J. Xu, Y.S. Meng, Phys. Chem. Chem. Phys. : Phys. Chem. Chem. Phys. 15 (2013) 3304.
[8] Y. Mo, S.P. Ong, G. Ceder, Chem. Mater. 26 (2014) 5208.
[9] a) O. Arcelus, J. Carrasco, ACS Appl. Mater. Interfaces 11 (2019) 12562;
b) L. Vitoux, M. Guignard, M.R. Suchomel, J.C. Pramudita, N. Sharma, C. Delmas, Chem. Mater. 29 (2017) 7243.
[10] a) F. Tournadre, L. Croguennec, I. Saadoune, D. Carlier, Y. Shao-Horn, P. Willmann, C. Delmas, J. Solid State Chem. 177 (2004) 2790;
b) S. Kumakura, Y. Tahara, K. Kubota, K. Chihara, S. Komaba, Angew. Chem. 55 (2016) 12760;
c) A. Kulka, C. Marino, K. Walczak, C. Borca, C. Bolli, P. Novák, C. Villevieille, J. Mater. Chem. A 8 (2020) 6022;
d) L. Liu, X. Li, S.-H. Bo, Y. Wang, H. Chen, N. Twu, Di Wu, G. Ceder, Adv. Energy Mater. 5 (2015) 1500944;
e) B. Mortemard de Boisse, D. Carlier, M. Guignard, L. Bourgeois, C. Delmas, Inorg. Chem. 53 (2014) 11197.
[11] K. Wang, P. Yan, M. Sui, Nano Energy 54 (2018) 148.
[12] C. Ma, J. Alvarado, J. Xu, R.J. Clément, M. Kodur, W. Tong, C.P. Grey, Y.S. Meng, J. Am. Chem. Soc. 139 (2017) 4835.
[13] a) C.S. Johnson, J.-S. Kim, C. Lefief, N. Li, J.T. Vaughey, M.M. Thackeray, Electrochem. Commun. 6 (2004) 1085;
b) G. Assat, J.-M. Tarascon, Nat. Energy 3 (2018) 373;
c) W. Lee, S. Yun, H. Li, J. Kim, H. Lee, K. Kwon, J.Y. Lee, Y.-M. Choi, W.-S. Yoon, Small 16 (2020) e1905875;
d) Y. Yu, P. Karayaylali, D. Sokaras, L. Giordano, R. Kou, C.-J. Sun, F. Maglia, R. Jung, F.S. Gittleson, Y. Shao-Horn, Energy Environ. Sci. 14 (2021) 2322.
[14] a) B. Mortemard de Boisse, S.-I. Nishimura, E. Watanabe, L. Lander, A. Tsuchimoto, J. Kikkawa, E. Kobayashi, D. Asakura, M. Okubo, A. Yamada, Adv. Energy Mater. 8 (2018) 1800409;
b) Y. Li, X. Wang, Y. Gao, Q. Zhang, G. Tan, Q. Kong, S. Bak, G. Lu, X.-Q. Yang, L. Gu, et al., Adv. Energy Mater. 9 (2019) 1803087;
c) G.-H. Lee, J. Wu, D. Kim, K. Cho, M. Cho, W. Yang, Y.-M. Kang, Angew. Chem. 59 (2020) 8681;
d) W. Kong, R. Gao, Q. Li, W. Yang, J. Yang, L. Sun, X. Liu, J. Mater. Chem. A 7 (2019) 9099;
e) X. Bai, M. Sathiya, B. Mendoza-Sánchez, A. Iadecola, J. Vergnet, R. Dedryvère, M. Saubanère, A.M. Abakumov, P. Rozier, J.-M. Tarascon, Adv. Energy Mater. 8 (2018) 1802379;
f) M. Jia, Y. Qiao, X. Li, F. Qiu, X. Cao, P. He, H. Zhou, ACS Appl. Mater. Interfaces 12 (2020) 851.
[15] M. Saubanère, E. McCalla, J.-M. Tarascon, M.-L. Doublet, Energy Environ. Sci. 9 (2016) 984.
[16] A. Konarov, J.U. Choi, Z. Bakenov, S.-T. Myung, J. Mater. Chem. A 6 (2018) 8558.
[17] a) H. Li, Z. Wang, L. Chen, X. Huang, Adv. Mater. 21 (2009) 4593;
b) A. Mauger, C. Julien, Ionics 20 (2014) 751.
[18] T.R. Somo, T.E. Mabokela, D.M. Teffu, T.K. Sekgobela, B. Ramogayana, M.J. Hato, K.D. Modibane, Coatings 11 (2021) 744.
[19] W. Yan, S. Yang, Y. Huang, Y. Yang, G. Yuan, J. Alloys Compd. 819 (2020) 153048.
[20] J. Cho, Y.J. Kim, T.-J. Kim, B. Park, Angew. Chem. Int. Ed. 40 (2001) 3367.
[21] H.V. Ramasamy, K. Kaliyappan, R. Thangavel, V. Aravindan, K. Kang, D.U. Kim, Y. Park, X. Sun, Y.-S. Lee, J. Mater. Chem. A 5 (2017) 8408.
[22] J.-Y. Hwang, T.-Y. Yu, Y.-K. Sun, J. Mater. Chem. A 6 (2018) 16854.
[23] J.-Z. Wang, Y.-X. Teng, G.-Q. Su, S. Bao, J.-L. Lu, J. Colloid Interface Sci. 608 (2022) 3013.
[24] a) W. Kong, H. Wang, L. Sun, C. Su, X. Liu, Appl. Surf. Sci. 497 (2019) 143814;
b) J. Alvarado, C. Ma, S. Wang, K. Nguyen, M. Kodur, Y.S. Meng, ACS Appl. Mater. Interfaces 9 (2017) 26518;
c) H.V. Ramasamy, P. N Didwal, S. Sinha, V. Aravindan, J. Heo, C.-J. Park, Y.-S. Lee, J. Colloid Interface Sci. 564 (2020) 467;
d) L. Zhao, J. Zhao, Y.-S. Hu, H. Li, Z. Zhou, M. Armand, L. Chen, Adv. Energy Mater. 2 (2012) 962;
e) X. Han, Y. Liu, Z. Jia, Y.-C. Chen, J. Wan, N. Weadock, K.J. Gaskell, T. Li, L. Hu, Nano Lett. 14 (2014) 139;
f) Y. Chang, G. Xie, Y. Zhou, J. Wang, Z. Wang, H. Guo, B. You, G. Yan, Trans. Nonferrous Metals Soc. China 32 (2022) 262;
g) C.-H. Jo, J.-H. Jo, H. Yashiro, S.-J. Kim, Y.-K. Sun, S.-T. Myung, Adv. Energy Mater. 8 (2018) 1702942;
h) J.H. Jo, J.U. Choi, A. Konarov, H. Yashiro, S. Yuan, L. Shi, Y.-K. Sun, S.-T. Myung, Adv. Funct. Mater. 28 (2018) 1705968;
i) H.-H. Sun, J.-Y. Hwang, C.S. Yoon, A. Heller, C.B. Mullins, ACS Nano 12 (2018) 12912;
j) K. Tang, Y. Huang, X. Xie, S. Cao, L. Liu, M. Liu, Y. Huang, B. Chang, Z. Luo, X. Wang, Chem. Eng. J. 384 (2020) 123234.
[25] Y. Liu, X. Fang, A. Zhang, C. Shen, Q. Liu, H.A. Enaya, C. Zhou, Nano Energy 27 (2016) 27.
[26] Y. Yang, R. Dang, K. Wu, Q. Li, N. Li, X. Xiao, Z. Hu, J. Phys. Chem. C 124 (2020) 1780.
[27] R. Dang, Q. Li, M. Chen, Z. Hu, X. Xiao, Phys. Chem. Chem. Phys. : Phys. Chem. Chem. Phys. 21 (2018) 314.
[28] H. Kim, J.-H. Park, S.-C. Kim, D. Byun, K.Y. Chung, H.-S. Kim, W. Choi, J. Alloys Compd. 856 (2021) 157294.
[29] C. Gauckler, M. Dillenz, F. Maroni, L.F. Pfeiffer, J. Biskupek, M. Sotoudeh, Q. Fu, U. Kaiser, S. Dsoke, H. Euchner, et al., ACS Appl. Energy Mater. (2022).
[30] L.F. Pfeiffer, N. Jobst, C. Gauckler, M. Lindén, M. Marinaro, S. Passerini, M. Wohlfahrt-Mehrens, P. Axmann, Front. Energy Res. (2022) 10.
[31] A.A. Abd-El-Latif, C.J. Bondue, S. Ernst, M. Hegemann, J.K. Kaul, M. Khodayari, E. Mostafa, A. Stefanova, H. Baltruschat, TrAC, Trends Anal. Chem. 70 (2015) 4.
[32] Y. Hoshino, T. Utsunomiya, O. Abe, BCSJ 54 (1981) 1385.
[33] a) R. Luo, F. Wu, M. Xie, Y. Ying, J. Zhou, Y. Huang, Y. Ye, L. Li, R. Chen, J. Power Sources 383 (2018) 80;
b) I. Hasa, D. Buchholz, S. Passerini, J. Hassoun, ACS Appl. Mater. Interfaces 7 (2015) 5206.
[34] A. Gutierrez, W.M. Dose, O. Borkiewicz, F. Guo, M. Avdeev, S. Kim, T.T. Fister, Y. Ren, J. Bareño, C.S. Johnson, J. Phys. Chem. C 122 (2018) 23251.
[35] S.-Y. Xu, X.-Y. Wu, Y.-M. Li, Y.-S. Hu, L.-Q. Chen, Chin. Phys. B 23 (2014) 118202.
[36] K.M. Shaju, G.V. Subba Rao, B.V.R. Chowdari, J. Electrochem. Soc. 151 (2004) A1324.
[37] T. Song, E. Kendrick, J. Phys. Mater. 4 (2021) 32004.
[38] W. Weppner, R.A. Huggins, J. Electrochem. Soc. 124 (1977) 1569.
[39] J. Jin, Y. Liu, X. Pang, Y. Wang, X. Xing, J. Chen, Sci. China Chem. 64 (2021) 385.
[40] A.T.S. Freiberg, M.K. Roos, J. Wandt, R. de Vivie-Riedle, H.A. Gasteiger, J. Phys. Chem. A 122 (2018) 8828.
[41] U. Maitra, R.A. House, J.W. Somerville, N. Tapia-Ruiz, J.G. Lozano, N. Guerrini, R. Hao, K. Luo, L. Jin, M.A. Pérez-Osorio, et al., Nat. Chem. 10 (2018) 288.
[42] M. Metzger, C. Marino, J. Sicklinger, D. Haering, H.A. Gasteiger, J. Electrochem. Soc. 162 (2015) A1123–A1134.
[43] X. Chen, N. Li, E. Kedzie, B.D. McCloskey, H. Tang, W. Tong, J. Electrochem. Soc. 166 (2019) A4136–A4140.
[44] M. Jia, H. Li, Y. Qiao, L. Wang, X. Cao, J. Cabana, H. Zhou, ACS Appl. Mater. Interfaces 12 (2020) 38249.
[45] Y. Zhang, M. Wu, J. Ma, G. Wei, Y. Ling, R. Zhang, Y. Huang, ACS Cent. Sci. 6 (2020) 232.
[46] Y. Wang, Z. Feng, P. Cui, W. Zhu, Y. Gong, M.-A. Girard, G. Lajoie, J. Trottier, Q. Zhang, L. Gu, et al., Nat. Commun. 12 (2021) 13.
[47] Y. Yu, de Ning, Q. Li, A. Franz, L. Zheng, N. Zhang, G. Ren, G. Schumacher, X. Liu, Energy Storage Mater. 38 (2021) 130.
[48] J. Wang, S.L. Dreyer, K. Wang, Z. Ding, T. Diemant, G. Karkera, Y. Ma, A. Sarkar, B. Zhou, M.V. Gorbunov, et al., Mater. Futures 1 (2022) 35104.
[49] B. Xiao, F. Omenya, D. Reed, X. Li, Nanotechnology (2021) 32.
[50] 10.5281/zenodo.8120332.